

Cite this: *Chem. Sci.*, 2025, 16, 8523

All publication charges for this article have been paid for by the Royal Society of Chemistry

# Interlayer engineering-induced charge redistribution in Bi<sub>2</sub>Te<sub>3</sub> toward efficient Zn<sup>2+</sup> and NH<sub>4</sub><sup>+</sup> storage†

Xiaojie Liang,<sup>a</sup> Fangzhong Liu,<sup>a</sup> Haonan Yue,<sup>a</sup> Yaoyong Dong,<sup>a</sup> Lijuan Chen,<sup>e</sup> Ting Song,<sup>id</sup> <sup>a</sup> Yong Pei,<sup>id</sup> <sup>a</sup> Xianyou Wang,<sup>id</sup> <sup>a</sup> Bei Long,<sup>id</sup> <sup>\*a</sup> Yao Xiao<sup>id</sup> <sup>\*cf</sup> and Xiongwei Wu<sup>id</sup> <sup>\*bd</sup>

Bismuth-based materials show promise for aqueous energy storage systems due to their unique layered structures and high storage capacity. Some bismuth-based materials have been applied to store Zn<sup>2+</sup> or NH<sub>4</sub><sup>+</sup>, indicating that one bismuth-based compound may be innovatively used in both zinc-ion and ammonium-ion batteries (ZIBs and AIBs). Herein, we successfully design a poly(3,4-ethylenedioxythiophene) (PEDOT) coated and embedded Bi<sub>2</sub>Te<sub>3</sub> (Bi<sub>2</sub>Te<sub>3</sub>@PEDOT). Theoretical calculations and experimental studies demonstrate that the PEDOT coating and its intercalation into the interlayer enhance the structural stability of Bi<sub>2</sub>Te<sub>3</sub> and significantly improve the storage capacities for Zn<sup>2+</sup> and NH<sub>4</sub><sup>+</sup>. The PEDOT intercalation results in an increased interlayer spacing and a charge redistribution in the interlayer, facilitating charge transfer. Additionally, the insertion-type mechanism of Zn<sup>2+</sup> and NH<sub>4</sub><sup>+</sup> in Bi<sub>2</sub>Te<sub>3</sub>@PEDOT is revealed through *ex situ* tests. The optimized electrode (5 mg cm<sup>-2</sup>) exhibits high discharge capacities of 385 mA h g<sup>-1</sup> in ZIBs and 235 mA h g<sup>-1</sup> in AIBs at 0.2 A g<sup>-1</sup> and long-term cycle stability. Bi<sub>2</sub>Te<sub>3</sub>@PEDOT performs robustly even at a high mass loading of 10 mg cm<sup>-2</sup>. Bi<sub>2</sub>Te<sub>3</sub>@PEDOT//MnO<sub>2</sub> (ZIBs) and Bi<sub>2</sub>Te<sub>3</sub>@PEDOT//ZnMn<sub>2</sub>O<sub>4</sub> (AIBs) full cells offer high reversible capacities. This work provides a reference for designing bifunctional energy storage materials.

Received 16th February 2025  
Accepted 4th April 2025

DOI: 10.1039/d5sc01210d

rsc.li/chemical-science

## Introduction

Aqueous batteries (ABs) are a new type of promising energy storage device due to their abundant raw materials, inherent safety, and high cost-effectiveness.<sup>1–5</sup> Various types of ABs have been developed such as Na<sup>+</sup>, K<sup>+</sup>, Al<sup>3+</sup>, Zn<sup>2+</sup>, Ca<sup>2+</sup>, H<sup>+</sup> and NH<sub>4</sub><sup>+</sup> ion batteries.<sup>6–9</sup> Among them, zinc-ion and ammonium-ion batteries (ZIBs and AIBs) have gained significant attention owing to the high theoretical specific capacity (5855 mA h cm<sup>-3</sup>)

of Zn anodes and the small hydrated ion size (0.331 nm) of NH<sub>4</sub><sup>+</sup>.<sup>10–13</sup> Though some materials have been reported to show good electrochemical performances in ZIBs and AIBs, such as MoO<sub>3</sub> and CuS, two different modification methods are essential to separately obtain high storage capacities for Zn<sup>2+</sup> and NH<sub>4</sub><sup>+</sup>.<sup>14–16</sup>

Recently, the design of bifunctional materials has been drawing more and more attention. For instance, Yu *et al.* synthesized a heterostructural VS<sub>2</sub>/VO<sub>x</sub> by an *in situ* electrochemical method; the VS<sub>2</sub>/VO<sub>x</sub> cathode displayed a high specific capacity of 156 mA h g<sup>-1</sup> at 10 A g<sup>-1</sup> in ZIBs and maintained a reversible capacity of 150 mA h g<sup>-1</sup> over more than 1000 cycles in AIBs.<sup>17</sup> Li and coworkers designed a layered NH<sub>4</sub>V<sub>4</sub>O<sub>10</sub> cathode with an adjustable interlayer distance through an *in situ* electrochemical strategy, and the optimized electrode exhibited good electrochemical performances for both Zn<sup>2+</sup> and NH<sub>4</sub><sup>+</sup> storage.<sup>18</sup> However, there are few reports on bifunctional anodes for both ZIBs and AIBs.

In previous works, layered bismuth-based materials such as BiOXs, Bi<sub>2</sub>O<sub>2</sub>CO<sub>3</sub>, and Bi<sub>2</sub>SeO<sub>5</sub> exhibited good Zn<sup>2+</sup> or NH<sub>4</sub><sup>+</sup> storage properties due to their large interlayer spacings and robust crystal structures.<sup>19–21</sup> Therefore, bismuth-based materials show great potential for both Zn<sup>2+</sup> and NH<sub>4</sub><sup>+</sup> storage. To achieve excellent electrochemical properties in bismuth-based materials, it is very important to improve electronic/ionic

<sup>a</sup>School of Chemistry, Xiangtan University, Xiangtan, 411105 Hunan, P. R. China. E-mail: longbei@xtu.edu.cn

<sup>b</sup>School of Chemistry and Materials Science, Hunan Agricultural University, Changsha, 410128 Hunan, P. R. China. E-mail: wxw@hunau.edu.cn

<sup>c</sup>College of Chemistry and Materials Engineering, Wenzhou University, Wenzhou, 325035 Zhejiang, P. R. China. E-mail: xiaoyao@wzu.edu.cn

<sup>d</sup>College of Chemistry and Chemical Engineering, National & Local Joint Engineering Laboratory for New Petro-chemical Materials and Fine Utilization of Resources, Hunan Normal University, Changsha, 410081 Hunan, P. R. China

<sup>e</sup>College of Intelligent Science and Engineering, Hunan Institute of Engineering, Xiangtan 411104 Hunan, P. R. China

<sup>f</sup>Key Laboratory of Advanced Energy Materials Chemistry (Ministry of Education), Nankai University, Tianjin 300071, P. R. China

† Electronic supplementary information (ESI) available: Experimental section, crystallography data and additional figures. See DOI: <https://doi.org/10.1039/d5sc01210d>

conductivity.<sup>22,23</sup> Doping/defect engineering is often used to promote electronic rearrangement and therefore enhances ion/electron transfer, such as Co-doped BiOBr and Se vacancy-activated Bi<sub>2</sub>Se<sub>3</sub>.<sup>20,24</sup> However, localized or uneven doping and defects result in their restricted enhancement. For instance, excessive Co doping increases the diffusion barrier in a local area.<sup>20</sup> Moreover, the designs of the coating and composite can only improve electron or ion transfer. Fortunately, interlayer engineering is a good choice for layered materials. Benefiting from the existence of structural pillars (cations, graphene, polymers and so on), the interlamellar spacing is increased and the electrostatic interaction between layers is decreased, enabling fast reversible ion diffusion/intercalation and high structural stability.<sup>25–27</sup>

In this study, we prepare a PEDOT-coated/embedded Bi<sub>2</sub>Te<sub>3</sub> (Bi<sub>2</sub>Te<sub>3</sub>@PEDOT) as a bifunctional anode material for efficient Zn<sup>2+</sup> and NH<sub>4</sub><sup>+</sup> storage. The coating of PEDOT improves the stability and electronic conductivity of Bi<sub>2</sub>Te<sub>3</sub>, and the embedded PEDOT changes the interlayer spacing and charge distribution of Bi<sub>2</sub>Te<sub>3</sub> and thus enhances Zn<sup>2+</sup>/NH<sub>4</sub><sup>+</sup> transport kinetics. The Bi<sub>2</sub>Te<sub>3</sub>@PEDOT electrode shows superior capacity for Zn<sup>2+</sup> and NH<sub>4</sub><sup>+</sup> storage at mass loadings of 5 and 10 mg cm<sup>-2</sup>. Remarkably, Zn<sup>2+</sup> and NH<sub>4</sub><sup>+</sup> full cells also display satisfactory discharge capacity and cycling stability.

## Results and discussion

The preparation processes of Bi<sub>2</sub>Te<sub>3</sub> and Bi<sub>2</sub>Te<sub>3</sub>@PEDOT are schematically displayed in Fig. 1a. Firstly, hexagonal Bi<sub>2</sub>Te<sub>3</sub> nanosheets are synthesized *via* a solvothermal method, and then PEDOT is coated on and embedded in Bi<sub>2</sub>Te<sub>3</sub> during the polymerization process of EDOT. The compositions and distinctions of Bi<sub>2</sub>Te<sub>3</sub> and Bi<sub>2</sub>Te<sub>3</sub>@PEDOT are characterized by various tests. The X-ray diffraction (XRD) patterns reveal that both samples exhibit similar characteristic peaks which are consistent with Bi<sub>2</sub>Te<sub>3</sub> (JCPDS no. 15-0863), suggesting that the crystal structure of Bi<sub>2</sub>Te<sub>3</sub> remains unchanged after the incorporation of PEDOT (Fig. 1b). Significantly, the (006) crystal plane in Bi<sub>2</sub>Te<sub>3</sub>@PEDOT (17.22°) shifts to a low angle compared to Bi<sub>2</sub>Te<sub>3</sub> (17.48°), indicating that the lattice spacing increases from 0.507 to 0.515 nm due to the insertion of PEDOT (inset of Fig. 1b). The pure PEDOT is characterized by means of multiple methods (Fig. S1†). Raman spectra further confirm the presence of both Bi<sub>2</sub>Te<sub>3</sub> and PEDOT in Bi<sub>2</sub>Te<sub>3</sub>@PEDOT (Fig. 1c). The peaks at 62, 102, and 134 cm<sup>-1</sup> arise from the A<sub>1g</sub>, E<sub>2g</sub>, and A<sub>2g</sub> modes of Bi<sub>2</sub>Te<sub>3</sub>, while the characteristic peaks of PEDOT are located at 990, 1263, 1365, 1435, 1510, and 1566 cm<sup>-1</sup>.<sup>27–29</sup> Additionally, the peaks in Bi<sub>2</sub>Te<sub>3</sub>@PEDOT exhibit a visible red shift (inset in Fig. 1c). X-ray photoelectron spectroscopy (XPS) is employed to analyze the chemical state of Bi<sub>2</sub>Te<sub>3</sub> and Bi<sub>2</sub>Te<sub>3</sub>@PEDOT. In the Te 3d XPS spectra (Fig. 1d), the peaks at 571.8 and 582.2 eV in Bi<sub>2</sub>Te<sub>3</sub> originate from the Te–Bi bonds, and the Te–O bonds at 572.5 and 586.0 eV are attributed to surface oxidation.<sup>30</sup> Similarly, the peaks at 157.2/162.5 eV and 158.6/164.0 eV in the Bi 4f XPS spectra correspond to the Te–Bi and O–Bi bonds, respectively (Fig. S2a†).<sup>31,32</sup> However, those peaks in Bi<sub>2</sub>Te<sub>3</sub>@PEDOT shift towards higher binding energies,

indicating the change in the chemical environment due to the introduction of PEDOT. Further evidence for the successful synthesis of Bi<sub>2</sub>Te<sub>3</sub>@PEDOT is provided by the C 1s and S 2p XPS spectra and the Fourier-transform infrared (FT-IR) spectroscopy spectra (Fig. S2b–d†).<sup>33,34</sup> Nitrogen adsorption/desorption isotherms and pore size distribution curves reveal that the cumulative pore volume of Bi<sub>2</sub>Te<sub>3</sub> rises from 0.0395 to 0.1201 cm<sup>3</sup> g<sup>-1</sup>, and the specific surface area grows from 7.54 to 19.66 m<sup>2</sup> g<sup>-1</sup> after the introduction of PEDOT (Fig. S3†).

Scanning electron microscopy (SEM) and transmission electron microscopy (TEM) images provide insights into the microstructure and morphology of the samples. The SEM image reveals that Bi<sub>2</sub>Te<sub>3</sub> exhibits a smooth hexagonal nanosheet structure (Fig. 1e). Conversely, Bi<sub>2</sub>Te<sub>3</sub>@PEDOT displays a rough surface, due to the PEDOT coating layer (Fig. 1f). This explains the increased specific surface area in Bi<sub>2</sub>Te<sub>3</sub>@PEDOT and enhances the charge transfer between Bi<sub>2</sub>Te<sub>3</sub>@PEDOT and electrolyte. The TEM images reveal a PEDOT coating layer with a thickness of approximately 10 nm in Bi<sub>2</sub>Te<sub>3</sub>@PEDOT (Fig. S4a and b†). The high-resolution TEM (HRTEM) image exhibits the lattice fringes (0.383 nm) which corresponds to the (101) crystal plane of Bi<sub>2</sub>Te<sub>3</sub> (greater than 0.377 nm for pure Bi<sub>2</sub>Te<sub>3</sub>) (Fig. 1g).<sup>35</sup> This result corresponds to the shift in the XRD test. Simultaneously, the polycrystalline nature of Bi<sub>2</sub>Te<sub>3</sub>@PEDOT is confirmed by the selected area electron diffraction (SAED) test (Fig. S4c†). Elemental mapping illustrates that Bi, Te, S, O, and C elements are evenly distributed across the nanosheet (Fig. 1h). The above results demonstrate the successful synthesis of Bi<sub>2</sub>Te<sub>3</sub> and Bi<sub>2</sub>Te<sub>3</sub>@PEDOT.

Density functional theory (DFT) calculations are used to investigate the role of the embedded PEDOT in the Bi<sub>2</sub>Te<sub>3</sub> structure. The optimized crystal structures of Bi<sub>2</sub>Te<sub>3</sub> (8.87 × 15.38 × 30.55 Å, α = 90.15°, β = 90°, γ = 90°) and PEDOT-Bi<sub>2</sub>Te<sub>3</sub> (8.94 × 15.44 × 37.96 Å, α = 90.09°, β = 90.03°, γ = 89.98°) are presented in Fig. S5.† The insertion of PEDOT results in an expanded interlayer distance and a slight lattice distortion, which is consistent with the experimental results. Differential charge distribution diagrams reveal significant interlamellar electron exchange in the Bi<sub>2</sub>Te<sub>3</sub>, reflecting a strong interaction in the interlayer (Fig. 1i). PEDOT intercalation reduces such electron exchange, weakening the interlayer interaction (Fig. 1j). Bader charge analysis further supports this finding. Specifically, the average electron count of Te atoms adjacent to PEDOT decreases from 0.37 (without PEDOT) to 0.06 e, indicating that more electron transfer occurs between PEDOT and its neighboring Te atoms. The density of states (DOS) is simulated for both Bi<sub>2</sub>Te<sub>3</sub> and PEDOT-Bi<sub>2</sub>Te<sub>3</sub> (Fig. S6†). The Bi<sub>2</sub>Te<sub>3</sub> model exhibits typical semiconductor properties. The downward shift of the DOS peaks in the PEDOT-Bi<sub>2</sub>Te<sub>3</sub> model along with the significant DOS at the Fermi level indicates a transformation from semiconductor to conductor, suggesting that the insertion of PEDOT significantly improves the electrical conductivity of PEDOT-Bi<sub>2</sub>Te<sub>3</sub>.<sup>36</sup> The reduced interlayer electronic interactions and improved electrical conductivity are expected to facilitate ion diffusion in the interlayer, therefore enhancing the electrochemical performances of Bi<sub>2</sub>Te<sub>3</sub>@PEDOT.



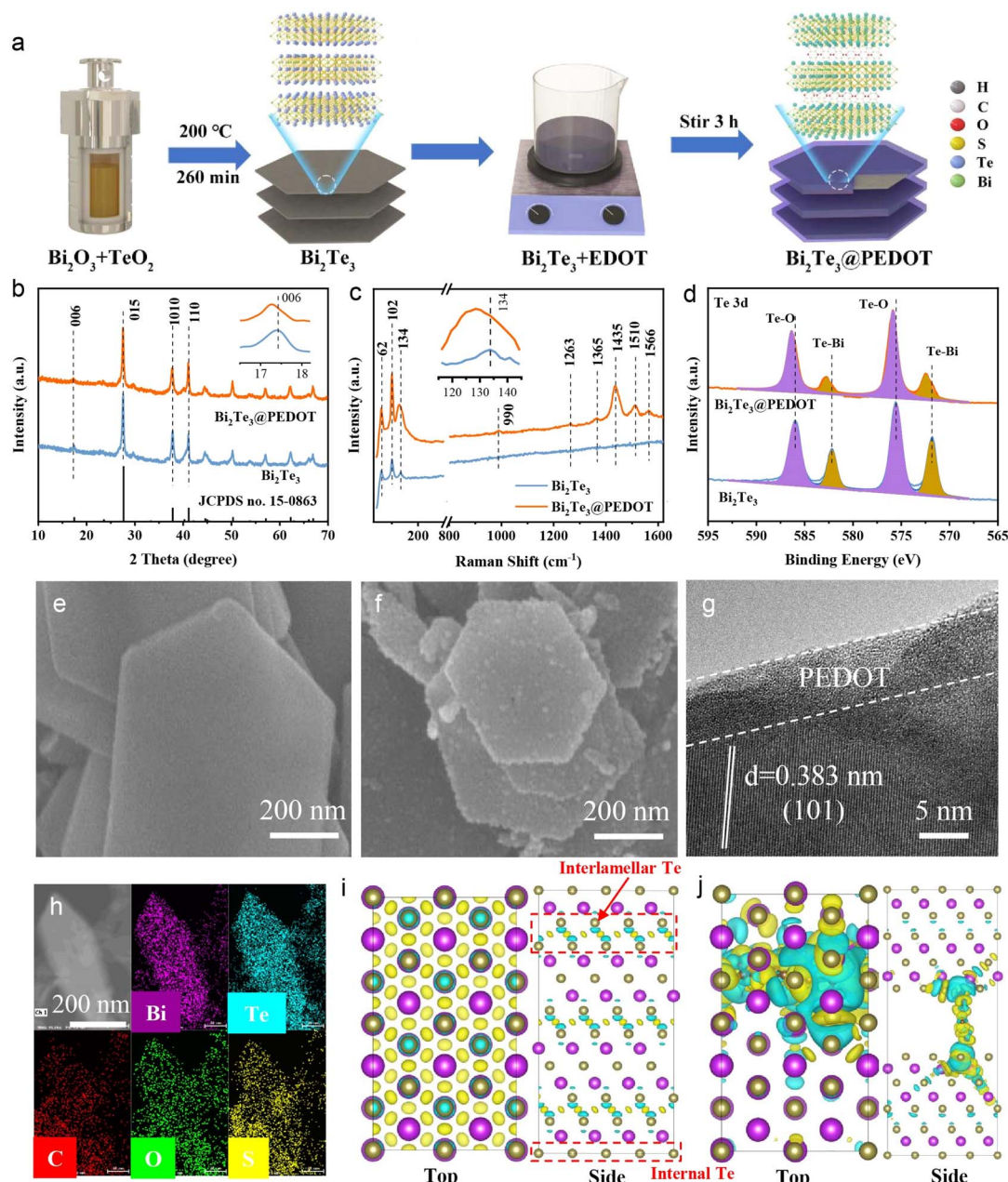


Fig. 1 (a) Schematic diagram of the preparation of  $\text{Bi}_2\text{Te}_3$  and  $\text{Bi}_2\text{Te}_3@\text{PEDOT}$ . (b) XRD patterns, (c) Raman spectra, and (d) Te 3d XPS spectra of  $\text{Bi}_2\text{Te}_3$  and  $\text{Bi}_2\text{Te}_3@\text{PEDOT}$ . SEM images of (e)  $\text{Bi}_2\text{Te}_3$  and (f)  $\text{Bi}_2\text{Te}_3@\text{PEDOT}$ . (g) TEM images of  $\text{Bi}_2\text{Te}_3@\text{PEDOT}$ . (h) Elemental mapping of  $\text{Bi}_2\text{Te}_3@\text{PEDOT}$ . Charge density distributions of (i)  $\text{Bi}_2\text{Te}_3$  and (j) PEDOT- $\text{Bi}_2\text{Te}_3$  (the purple and brown colors represent Bi and Te atoms, and the yellow and blue regions reflect electron accumulation and electron depletion, respectively).

The electrochemical properties of  $\text{Bi}_2\text{Te}_3$  and  $\text{Bi}_2\text{Te}_3@\text{PEDOT}$  in ZIBs are evaluated firstly. In cyclic voltammetry (CV) tests,  $\text{Bi}_2\text{Te}_3$  exhibits two redox peaks at 0.62, 0.68, 1.15, and 1.20 V, suggesting the multi-step insertion/deinsertion of  $\text{Zn}^{2+}$  in  $\text{Bi}_2\text{Te}_3$ . Meanwhile,  $\text{Bi}_2\text{Te}_3@\text{PEDOT}$  shows a pair of redox peaks at  $\sim 0.6/1.2$  V, reflecting a variation in the insertion/deinsertion process of  $\text{Zn}^{2+}$  after the introduction of PEDOT (Fig. S7†).<sup>37</sup> This change is explored in the subsequent studies. Meanwhile, the first three CV curves of  $\text{Bi}_2\text{Te}_3@\text{PEDOT}$  overlap better than those of  $\text{Bi}_2\text{Te}_3$ , indicating its improved reversibility.

The first three galvanostatic charge–discharge (GCD) curves show an average discharge plateau at about 0.69 V in  $\text{Bi}_2\text{Te}_3$  and 0.67 V in  $\text{Bi}_2\text{Te}_3@\text{PEDOT}$ , implying their suitability as anodes in full cells (Fig. S8†). The rate performances and cycling properties are further explored. At current densities of 0.2, 0.5, 1.0, 2.0, 3.0, 5.0, and 10  $\text{A g}^{-1}$ ,  $\text{Bi}_2\text{Te}_3@\text{PEDOT}$  offers specific capacities of 378, 340, 320, 312, 310, 300, and 253  $\text{mA h g}^{-1}$ , significantly higher than those of  $\text{Bi}_2\text{Te}_3$  (195, 180, 152, 123, 110, 97, and 80  $\text{mA h g}^{-1}$ ) and PEDOT (Fig. 2a and S9†). Fig. 2b and c shows the GCD curves at different current densities, in which



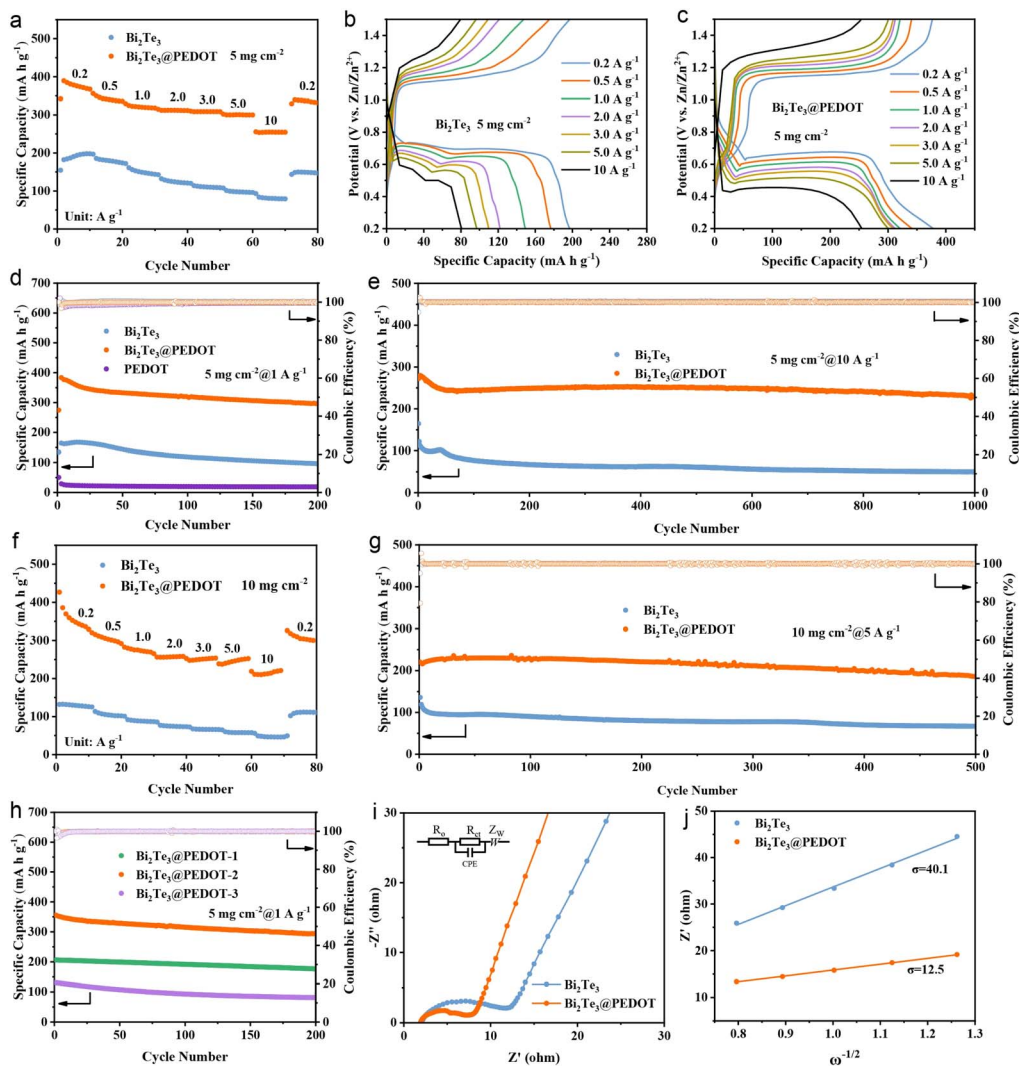


Fig. 2 (a) Rate performances and (b and c) corresponding GCD curves of  $\text{Bi}_2\text{Te}_3$  and  $\text{Bi}_2\text{Te}_3$ @PEDOT. (d) Cycle life of  $\text{Bi}_2\text{Te}_3$ ,  $\text{Bi}_2\text{Te}_3$ @PEDOT, and PEDOT at  $1 \text{ A g}^{-1}$ . (e) Cyclic performances of  $\text{Bi}_2\text{Te}_3$  and  $\text{Bi}_2\text{Te}_3$ @PEDOT at  $10 \text{ A g}^{-1}$  ( $5 \text{ mg cm}^{-2}$ ). (f) Rate capabilities and (g) cyclic performances of  $\text{Bi}_2\text{Te}_3$  and  $\text{Bi}_2\text{Te}_3$ @PEDOT at  $5 \text{ A g}^{-1}$  ( $10 \text{ mg cm}^{-2}$ ). (h) Cycle life of  $\text{Bi}_2\text{Te}_3$ @PEDOT- $x$  at  $1 \text{ A g}^{-1}$ . (i) EIS spectra and (j) relationship between  $\omega^{-1/2}$  and  $Z'$  of  $\text{Bi}_2\text{Te}_3$  and  $\text{Bi}_2\text{Te}_3$ @PEDOT.

$\text{Bi}_2\text{Te}_3$ @PEDOT exhibits more stable charging and discharging plateaus. In the cycle life test,  $\text{Bi}_2\text{Te}_3$ @PEDOT maintains a discharge capacity of  $295 \text{ mA h g}^{-1}$  after 200 cycles at  $1 \text{ A g}^{-1}$ , which is significantly higher than that of  $\text{Bi}_2\text{Te}_3$  ( $96 \text{ mA h g}^{-1}$ ) (Fig. 2d). Significantly, PEDOT exhibits a negligible  $\text{Zn}^{2+}$  storage capacity ( $18 \text{ mA h g}^{-1}$ ), reflecting its low capacity contribution to  $\text{Bi}_2\text{Te}_3$ @PEDOT. After 1000 cycles at  $10 \text{ A g}^{-1}$ ,  $\text{Bi}_2\text{Te}_3$ @PEDOT retains 82% of its initial capacity, while  $\text{Bi}_2\text{Te}_3$  retains only 40% (Fig. 2e). Additionally, the high mass loading  $\text{Bi}_2\text{Te}_3$ @PEDOT electrodes ( $10 \text{ mg cm}^{-2}$ ) are further tested. The discharge capacities of  $\text{Bi}_2\text{Te}_3$ @PEDOT are 325, 290, 263, 257, 253, 251, and  $219 \text{ mA h g}^{-1}$  at current densities from 0.2 to  $10 \text{ A g}^{-1}$ , much higher than those of  $\text{Bi}_2\text{Te}_3$  (125, 99, 85, 75, 64, 56, and  $49 \text{ mA h g}^{-1}$ ) (Fig. 2f). After 500 cycles at  $5 \text{ A g}^{-1}$ ,  $\text{Bi}_2\text{Te}_3$ @PEDOT maintains a discharge capacity of  $187 \text{ mA h g}^{-1}$ , while  $\text{Bi}_2\text{Te}_3$  retains only  $68 \text{ mA h g}^{-1}$  (Fig. 2g). The rate and cycling performances of  $\text{Bi}_2\text{Te}_3$ @PEDOT- $x$  are compared (Fig. 2h and S10†). It

is clear that  $\text{Bi}_2\text{Te}_3$ @PEDOT-2 ( $\text{Bi}_2\text{Te}_3$ @PEDOT) outperforms  $\text{Bi}_2\text{Te}_3$ @PEDOT-1 and  $\text{Bi}_2\text{Te}_3$ @PEDOT-3, reflecting that a suitable amount of PEDOT is critical to battery performance.

The electrochemical kinetics of  $\text{Bi}_2\text{Te}_3$  and  $\text{Bi}_2\text{Te}_3$ @PEDOT is analyzed by CV tests at different sweep rates (Fig. S11a and b†). Fitting the slopes of the  $\log(i)$  versus  $\log(v)$  curves (Fig. S11c†), the  $b$ -values of the redox peaks R1, O1, R2, and O2 are 0.72, 0.98, 0.62, and 0.67, respectively. This suggests the enhanced diffusion-controlled behavior of  $\text{Bi}_2\text{Te}_3$ @PEDOT due to its fast ion diffusion.<sup>38,39</sup> The electrochemical impedance spectra (EIS) show that the ohmic resistance ( $R_o = 2.13 \Omega$ ), charge transfer resistance ( $R_{ct} = 9.9 \Omega$ ), and Warburg factor ( $\sigma = 40.1$ ) of  $\text{Bi}_2\text{Te}_3$  are larger than those of  $\text{Bi}_2\text{Te}_3$ @PEDOT ( $R_o = 1.94 \Omega$ ,  $R_{ct} = 4.56 \Omega$ , and  $\sigma = 16.8$ ), thereby indicating an improved reaction kinetics in  $\text{Bi}_2\text{Te}_3$ @PEDOT (Fig. 2i and j). To further demonstrate the superiority of  $\text{Bi}_2\text{Te}_3$ @PEDOT, the  $\text{Zn}^{2+}$  diffusion coefficient is calculated by the galvanostatic intermittent

titration technique (GITT) test and Fick's second law. As shown in Fig. S12,<sup>†</sup> the ion diffusion rate in  $\text{Bi}_2\text{Te}_3\text{@PEDOT}$  is larger than that in  $\text{Bi}_2\text{Te}_3$ . This result is attributed to the interlayer expansion and reduced electrostatic interaction of  $\text{Bi}_2\text{Te}_3$  and thus the improved ion diffusion rate.<sup>40</sup>

To explore the storage mechanism in  $\text{Bi}_2\text{Te}_3$  and  $\text{Bi}_2\text{Te}_3\text{@PEDOT}$ , *ex situ* XRD, XPS, and SEM are conducted. *Ex situ* XRD profiles of  $\text{Bi}_2\text{Te}_3$  and  $\text{Bi}_2\text{Te}_3\text{@PEDOT}$  are displayed in Fig. 3a–d. Both materials maintain similar XRD patterns during the charge and discharge processes, indicating their intercalation/deintercalation mechanism. The (006) crystal plane in  $\text{Bi}_2\text{Te}_3$  shifts to a higher angle after the electrode is discharged to 0.2 V, which results from strong electrostatic interactions between the embedded  $\text{Zn}^{2+}$  and  $\text{Bi}_2\text{Te}_3$  layers (Fig. 3b).<sup>41</sup> In contrast, the (006) crystal plane of  $\text{Bi}_2\text{Te}_3\text{@PEDOT}$  shifts to a lower angle at the fully discharged state. This opposite result is attributed to the insertion of PEDOT and the enlarged interlayer spacing which reduces the interaction forces between  $\text{Zn}^{2+}$  and  $\text{Bi}_2\text{Te}_3$  layers (this is proved by DFT calculations).<sup>42</sup> Meanwhile, the by-product of  $\text{Zn}_4\text{SO}_4(\text{OH})_6 \cdot 4\text{H}_2\text{O}$  (ZSH) is generated in both  $\text{Bi}_2\text{Te}_3$  and  $\text{Bi}_2\text{Te}_3\text{@PEDOT}$ , though the intensity of ZSH peaks is weak in  $\text{Bi}_2\text{Te}_3\text{@PEDOT}$ . To assess the stability of the materials,  $\text{Bi}_2\text{Te}_3$  and  $\text{Bi}_2\text{Te}_3\text{@PEDOT}$  are soaked in 2 mol  $\text{L}^{-1}$   $\text{ZnSO}_4$  electrolyte for 2 h. As shown in Fig. S13a,<sup>†</sup> numerous bubbles

are clearly observed on the surface of  $\text{Bi}_2\text{Te}_3$ , and some white by-products appear on  $\text{Bi}_2\text{Te}_3$  after drying. In contrast, there is no obvious change for  $\text{Bi}_2\text{Te}_3\text{@PEDOT}$ . In addition, the XRD pattern of  $\text{Bi}_2\text{Te}_3$  shows the peaks of  $\text{Bi}_2\text{TeO}_5$  and  $\text{Zn}(\text{SO}_4)(\text{H}_2\text{O})_6$ , whereas no obvious new phase is detected in  $\text{Bi}_2\text{Te}_3\text{@PEDOT}$  (Fig. S13b<sup>†</sup>).

The energy storage mechanism is further investigated using *ex situ* XPS spectra. In the Bi 4f spectra of  $\text{Bi}_2\text{Te}_3$  (Fig. 3e), the peaks of the Bi–O and Bi–Te bonds irreversibly shift to high binding energy during the first cycle, and the Bi–Te peaks almost disappear at the fully charged state. Moreover, Te–O and Te–Bi peaks in the Te 3d XPS spectra also exhibit similar change, implying the poor reversibility and stability of  $\text{Bi}_2\text{Te}_3$  (Fig. 3f). For comparison, those peaks in  $\text{Bi}_2\text{Te}_3\text{@PEDOT}$  do not change significantly during the reaction, highlighting its enhanced stability due to the coating and insertion of PEDOT (Fig. 3g and h). In the Zn 2p XPS spectra, no Zn signal is observed at the original state (Fig. S14<sup>†</sup>). Zn 2p peaks emerge when the electrode is discharged to 0.2 V and become weak at the fully charged state, indicating the  $\text{Zn}^{2+}$  intercalation/deintercalation.<sup>37,43</sup> The O 1s XPS spectra can be divided into two peaks: the O–H peak at 532.0 eV and the O–Bi/O–Te peak at 530.5 eV (Fig. S15<sup>†</sup>).<sup>44</sup> The area ratios of O–H and O–Bi/O–Te peaks increase and decrease in the discharge and charge

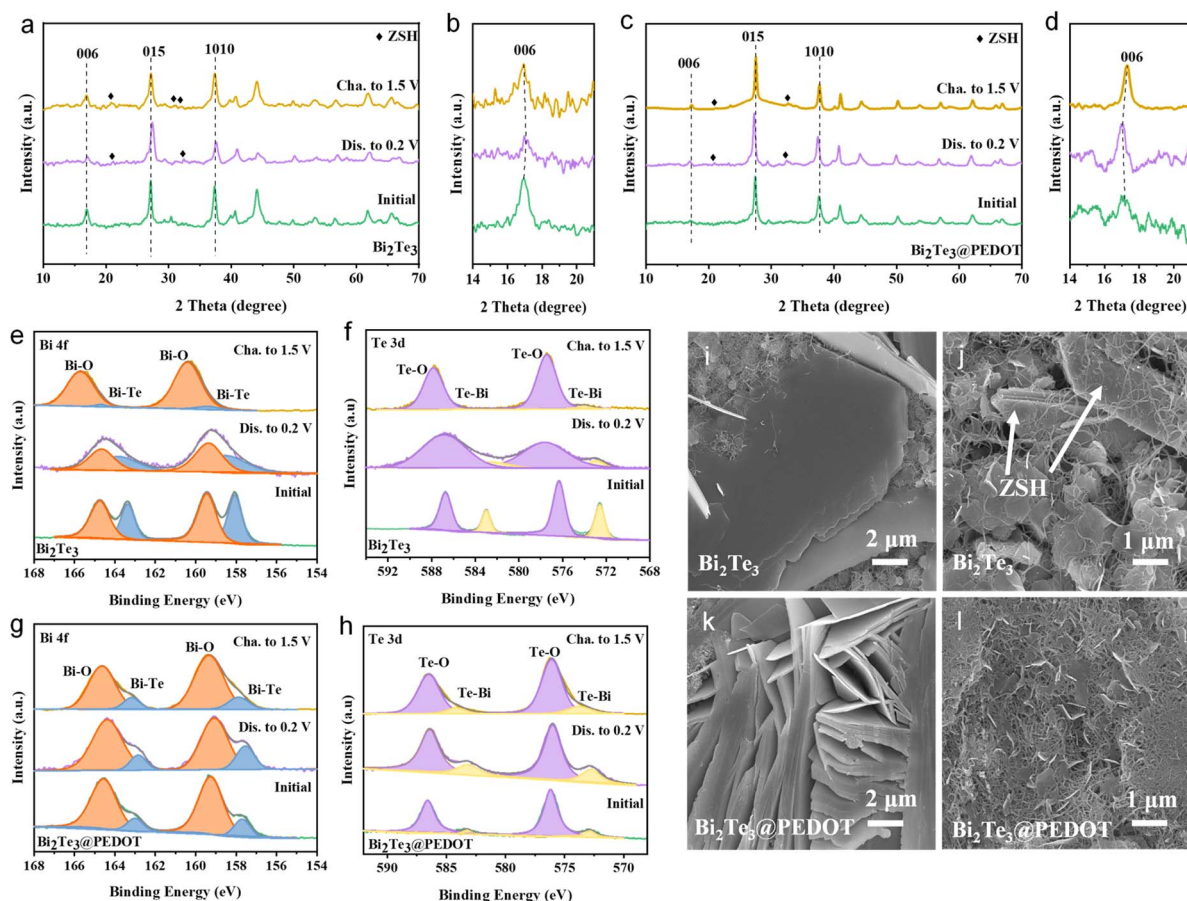


**Fig. 3** (a–d) *Ex situ* XRD patterns, (e and g) Bi 4f XPS spectra, and (f and h) Te 3d XPS spectra of  $\text{Bi}_2\text{Te}_3$  and  $\text{Bi}_2\text{Te}_3\text{@PEDOT}$ . SEM images of (i and j)  $\text{Bi}_2\text{Te}_3$  and (k and l)  $\text{Bi}_2\text{Te}_3\text{@PEDOT}$  at the fully discharged/charged states.



processes, respectively, indicating the insertion/extraction of  $H^+$ . The discharge capacities of  $H^+$  and  $Zn^{2+}$  in  $Bi_2Te_3@PEDOT$  are studied in  $ZnSO_4/DMSO$  and  $H_2SO_4$  (pH = 5) electrolytes, respectively (Fig. S16<sup>†</sup>). The specific discharge capacity of  $H^+$  (194  $mA\ h\ g^{-1}$ ) is higher than that of  $Zn^{2+}$  (103  $mA\ h\ g^{-1}$ ), indicating dominant  $H^+$  storage. Additionally, the morphology changes of the electrodes at different charge states are observed by *ex situ* SEM. Many large-sized ZSH flakes are observed in both  $Bi_2Te_3$  and  $Bi_2Te_3@PEDOT$  at 0.2 V (Fig. 3i and k). The ZSH flakes are still visible in  $Bi_2Te_3$  at the fully charged state (Fig. 3j). Meanwhile, the ZSH almost disappears in  $Bi_2Te_3@PEDOT$ , implying its enhanced reaction reversibility (Fig. 3l). The above study demonstrates the co-insertion mechanism of  $Zn^{2+}$  and  $H^+$  in both  $Bi_2Te_3$  and  $Bi_2Te_3@PEDOT$ .  $Bi_2Te_3@PEDOT$  shows high stability and reversibility in the  $Zn^{2+}/H^+$  insertion/deinsertion processes.

The remarkable performances of  $Bi_2Te_3@PEDOT$  in ZIBs prompt an exploration of its electrochemical properties in AIBs.  $Bi_2Te_3@PEDOT$  exhibits good rate performance with specific capacities of 266, 235, 200, 164, and 113  $mA\ h\ g^{-1}$  at 0.1, 0.2, 0.5, 1.0, and 2.0  $A\ g^{-1}$ , respectively, which is higher than those of  $Bi_2Te_3$  (245, 212, 168, 120, and 71  $mA\ h\ g^{-1}$ ) (Fig. 4a). The corresponding GCD curves are displayed in Fig. S17<sup>†</sup> and  $Bi_2Te_3@PEDOT$  exhibits more obvious discharge plateaus at all current densities.  $Bi_2Te_3@PEDOT$  and  $Bi_2Te_3$  deliver the

discharge capacities of 156 and 113  $mA\ h\ g^{-1}$  with capacity retentions of 72% and 67%, respectively, after 700 cycles at 1  $A\ g^{-1}$  (Fig. 4b). Notably, PEDOT shows a low  $NH_4^+$  storage capacity, suggesting its low capacity contribution to  $Bi_2Te_3@PEDOT$  (Fig. S18<sup>†</sup>). Additionally,  $Bi_2Te_3$  and  $Bi_2Te_3@PEDOT$  electrodes are tested under a high mass loading of 10  $mg\ cm^{-2}$ . The discharge capacities of  $Bi_2Te_3@PEDOT$  are 257, 219, 169, 112, and 50  $mA\ h\ g^{-1}$  at current densities from 0.1 to 2.0  $A\ g^{-1}$ , while  $Bi_2Te_3$  exhibits lower discharge capacities (Fig. 4c). After 300 cycles at 1.0  $A\ g^{-1}$ ,  $Bi_2Te_3@PEDOT$  exhibits a significantly higher discharge capacity of 115  $mA\ h\ g^{-1}$  than that of  $Bi_2Te_3$  (66  $mA\ h\ g^{-1}$ ) (Fig. 4d). Evidently,  $Bi_2Te_3@PEDOT$  is well suited for use as a host material for  $NH_4^+$  storage.

The reaction kinetics of  $Bi_2Te_3$  and  $Bi_2Te_3@PEDOT$  is further investigated through CV, EIS, and GITT tests. In the first five CV curves, the redox peaks of  $Bi_2Te_3@PEDOT$  are more obvious, suggesting its higher capacity for  $NH_4^+$  storage (Fig. S19<sup>†</sup>). The corresponding *b*-values for peaks R1, O1, R2, and O2 are 0.67, 0.77, 0.83, and 0.74 respectively, suggesting an increased capacitive contribution of  $Bi_2Te_3@PEDOT$  (Fig. S20<sup>†</sup>). The  $R_{ct}$  and Warburg factor of  $Bi_2Te_3@PEDOT$  (68  $\Omega$  and 38.2) are significantly lower than those of  $Bi_2Te_3$  (108  $\Omega$  and 57.6), implying its enhanced charge transport (Fig. 4e and f). The GITT results also reveal the fast insertion and extraction rates of  $NH_4^+$  in  $Bi_2Te_3@PEDOT$  (Fig. S21<sup>†</sup>). The above results suggest the

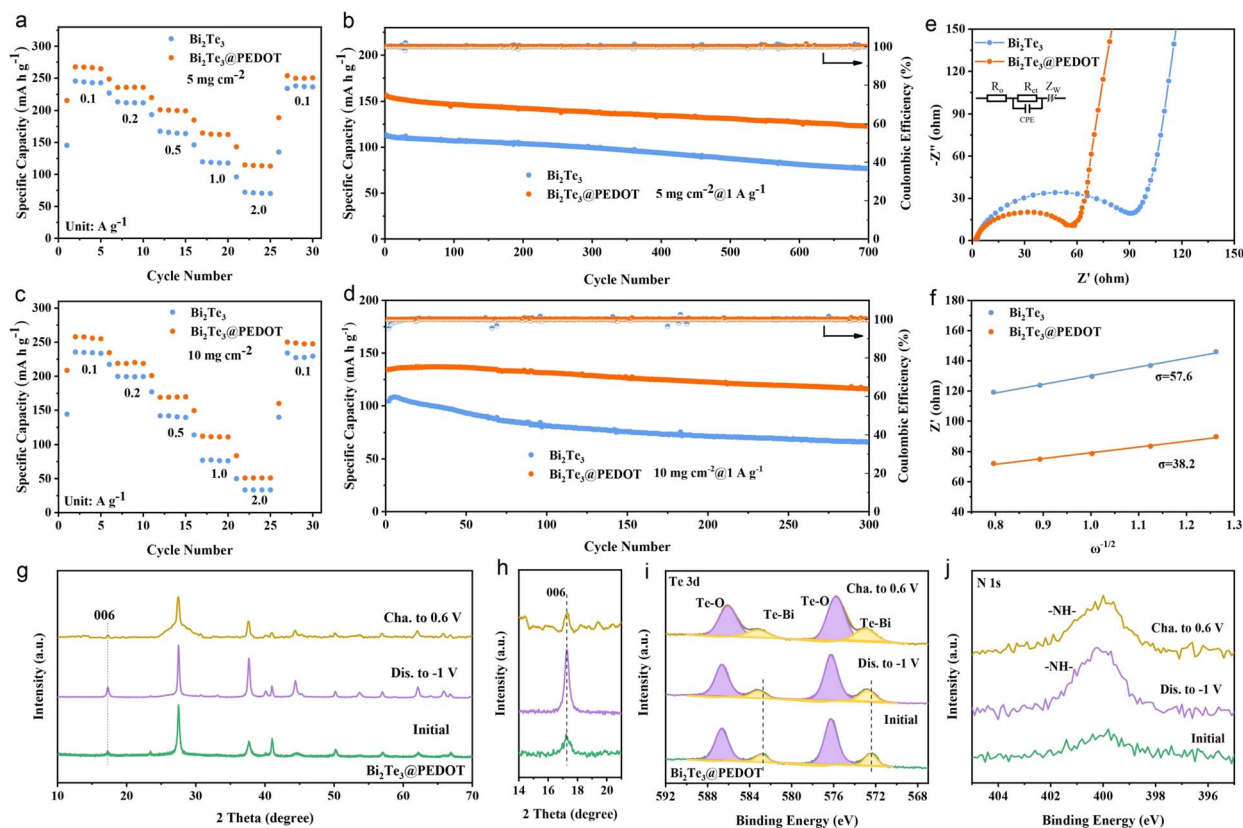


Fig. 4 (a) Rate performances and (b) cycle life of  $Bi_2Te_3$  and  $Bi_2Te_3@PEDOT$  (5  $mg\ cm^{-2}$ ) at 1  $A\ g^{-1}$ . (c) Rate capabilities and (d) cycle life of  $Bi_2Te_3$  and  $Bi_2Te_3@PEDOT$  (10  $mg\ cm^{-2}$ ) at 1  $A\ g^{-1}$ . (e) EIS spectra and (f) relationship between  $Z'$  and  $\omega^{-1/2}$  of  $Bi_2Te_3$  and  $Bi_2Te_3@PEDOT$ . (g and h) *Ex situ* XRD patterns, (i) Te 3d XPS spectra, and (j) N 1s XPS spectra of  $Bi_2Te_3@PEDOT$ .



improved charge transfer of  $\text{Bi}_2\text{Te}_3$  after the introduction of PEDOT.

To study the  $\text{NH}_4^+$  storage mechanism in  $\text{Bi}_2\text{Te}_3$ @PEDOT, *ex situ* XRD and XPS tests are conducted. The XRD test reveals that no new phase appears after the electrode is fully discharged/charged (Fig. 4g). The partial enlargement of the XRD pattern is shown in Fig. 4h, in which the (006) crystal plane remains

stable, implying that the insertion and extraction of  $\text{NH}_4^+$  do not affect the structure of  $\text{Bi}_2\text{Te}_3$ @PEDOT. This good stability is due to the protective layer of PEDOT and the increased interlayer spacing in  $\text{Bi}_2\text{Te}_3$ @PEDOT. As exhibited in Bi 4f and Te 3d XPS spectra, the Bi-Te peaks shift to higher binding energies after discharging, while the peak positions remain unchanged after charging, indicating a degree of irreversible reaction in the first

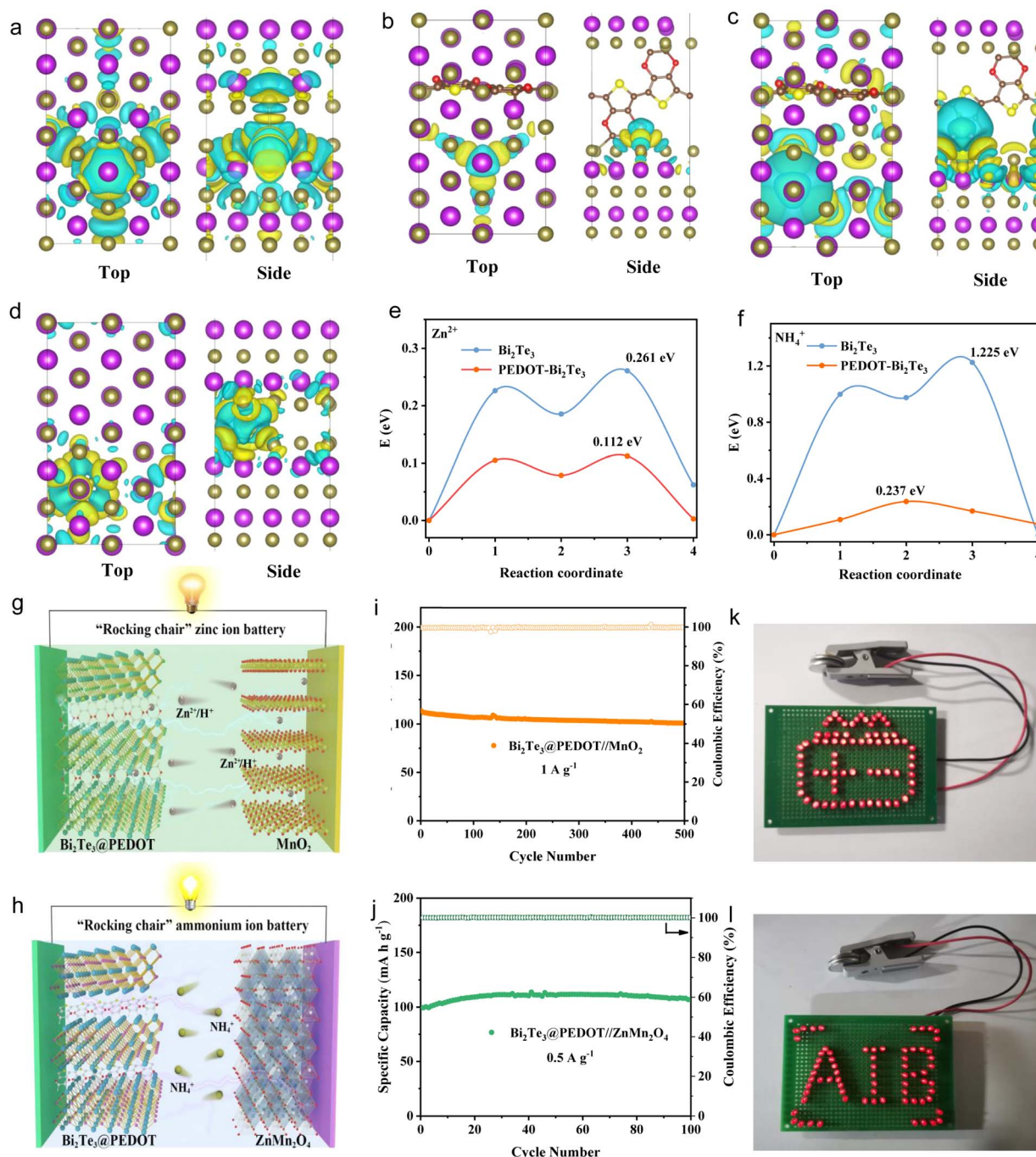


**Fig. 5** Charge density distributions of (a)  $\text{Bi}_2\text{Te}_3 + \text{Zn}^{2+}$ , (b) PEDOT- $\text{Bi}_2\text{Te}_3 + \text{Zn}^{2+}$ , (c)  $\text{Bi}_2\text{Te}_3 + \text{NH}_4^+$ , and (d) PEDOT- $\text{Bi}_2\text{Te}_3 + \text{NH}_4^+$  (the purple and brown colors represent Bi and Te atoms, and the yellow and blue regions reflect electron accumulation and electron depletion, respectively). (e)  $\text{Zn}^{2+}$  and (f)  $\text{NH}_4^+$  diffusion barriers of  $\text{Bi}_2\text{Te}_3$  and PEDOT- $\text{Bi}_2\text{Te}_3$ . (g and h) Structural illustration and (i and j) cycle life of  $\text{Bi}_2\text{Te}_3$ @PEDOT// $\text{MnO}_2$  and  $\text{Bi}_2\text{Te}_3$ @PEDOT// $\text{ZnMn}_2\text{O}_4$  full cells. Digital photos of two (k)  $\text{Bi}_2\text{Te}_3$ @PEDOT// $\text{MnO}_2$  and (l)  $\text{Bi}_2\text{Te}_3$ @PEDOT// $\text{ZnMn}_2\text{O}_4$  full cells lighting up red LEDs.



cycle (Fig. 4i and S22a†). In the N 1s spectra, a strong peak of –NH– appears at the fully discharged state, providing evidence that  $\text{NH}_4^+$  inserts into  $\text{Bi}_2\text{Te}_3$ @PEDOT (Fig. 4j). However, a weakened peak can still be seen after charging, reflecting the incomplete extraction of  $\text{NH}_4^+$ .<sup>17,45</sup> The intensity of O–H bonds in the O 1s spectra is enhanced after discharging and decreased after charging, demonstrating the co-insertion of  $\text{H}_2\text{O}$  along with  $\text{NH}_4^+$  (Fig. S22b†).<sup>45,46</sup> The above results prove the insertion of  $\text{NH}_4^+$  into  $\text{Bi}_2\text{Te}_3$ @PEDOT. Significantly,  $\text{Bi}_2\text{Te}_3$ @PEDOT outperforms most of the reported anodes in both ZIBs and AIBs (Tables S1 and S2†). Moreover, the high mass loading anode has been reported rarely.

The  $\text{Zn}^{2+}$  and  $\text{NH}_4^+$  storage properties of  $\text{Bi}_2\text{Te}_3$ , as well as the function of the embedded PEDOT, are further validated by DFT calculations. The ionic transport is affected by adsorption energy and lattice distortion. The charge density distributions are used to reveal the effect of PEDOT insertion on  $\text{Zn}^{2+}$  and  $\text{NH}_4^+$  adsorption. In the PEDOT- $\text{Bi}_2\text{Te}_3$  model, the charge transfer between  $\text{Zn}^{2+}$  and surrounding Te atoms is reduced, leading to a change in adsorption energy from  $-0.547$  ( $\text{Bi}_2\text{Te}_3$ ) to  $-0.492$  eV (PEDOT- $\text{Bi}_2\text{Te}_3$ ) (Fig. 5a and b). This is beneficial to  $\text{Zn}^{2+}$  diffusion. According to Bader charge analysis, when  $\text{Zn}^{2+}$  is inserted into  $\text{Bi}_2\text{Te}_3$ , the Zn transfers a charge of  $0.428$  e to  $\text{Bi}_2\text{Te}_3$ , and it drops to  $0.089$  e in PEDOT- $\text{Bi}_2\text{Te}_3$ . Meanwhile, the three neighboring Te atoms obtain an average electron number of  $0.046$  e before PEDOT intercalation, and it decreases to  $0.009$  e after PEDOT intercalation. This is consistent with the charge density distributions. By contrast, the adsorption energy between  $\text{NH}_4^+$  and Te atoms increases from  $-0.735$  ( $\text{Bi}_2\text{Te}_3$ ) to  $-2.204$  eV (PEDOT- $\text{Bi}_2\text{Te}_3$ ) (Fig. 5c and d). Bader charge analysis shows that  $\text{NH}_4^+$  transfers  $0.53$  e before PEDOT insertion and  $0.73$  e after PEDOT insertion, while the average electron numbers gained by the three neighboring Te atoms are  $0.028$  and  $0.131$  e, respectively, indicating the formation of strong covalent interactions between  $\text{NH}_4^+$  and  $\text{Bi}_2\text{Te}_3$  after the PEDOT insertion and the adverse  $\text{NH}_4^+$  diffusion. On the other hand, the average bond length of Te–Bi near the adsorption site of  $\text{Bi}_2\text{Te}_3$  is  $3.08$  Å and increases to  $3.15$  and  $3.27$  Å after  $\text{Zn}^{2+}$  and  $\text{NH}_4^+$  insertion. This change shows a decrease from  $3.07$  Å to  $3.07$  and  $3.10$  Å with the help of interlayer engineering, facilitating  $\text{Zn}^{2+}$  and  $\text{NH}_4^+$  diffusion. Further analysis of the  $\text{Zn}^{2+}$ / $\text{NH}_4^+$  diffusion barriers in  $\text{Bi}_2\text{Te}_3$  and PEDOT- $\text{Bi}_2\text{Te}_3$  reveals a significant reduction in diffusion barriers with the insertion of PEDOT. The diffusion pathways of  $\text{Zn}^{2+}$ / $\text{NH}_4^+$  are illustrated in Fig. S23.† Specifically, the  $\text{Zn}^{2+}$ / $\text{NH}_4^+$  diffusion barrier in  $\text{Bi}_2\text{Te}_3$  ( $1.225/0.237$  eV) declines to  $0.261/0.112$  eV with the help of PEDOT (Fig. 5e and f). This reflects that the insertion of PEDOT improves the diffusion of  $\text{Zn}^{2+}$ / $\text{NH}_4^+$  due to the combined influence of adsorption energy and lattice distortion.

Finally, full cells are assembled to investigate the practical application of  $\text{Bi}_2\text{Te}_3$ @PEDOT in both “rocking-chair” ZIBs and AIBs, respectively. Commercial  $\text{MnO}_2$  and  $\text{ZnMn}_2\text{O}_4$  are used as cathodes due to their low cost and high operating voltages. The schematics of  $\text{Bi}_2\text{Te}_3$ @PEDOT// $\text{MnO}_2$  and  $\text{Bi}_2\text{Te}_3$ @PEDOT// $\text{ZnMn}_2\text{O}_4$  full cells are shown in Fig. 5g and h, where  $\text{Zn}^{2+}/\text{H}^+$  or  $\text{NH}_4^+$  shuttles between the anode and cathode through the electrolyte. The zinc-ion full battery exhibits a high capacity of

$110 \text{ mA h g}^{-1}$  at  $1 \text{ A g}^{-1}$  and a capacity retention of 88% after 500 cycles (Fig. 5i). The ammonium-ion full battery delivers a discharge capacity of  $110 \text{ mA h g}^{-1}$  at  $0.5 \text{ A g}^{-1}$  and good cycling stability over 100 cycles (Fig. 5j). The GCD curves of the ZIB and AIB full cells are displayed in Fig. S24.† In addition, both full cells drive the self-assembled red LED logos (Fig. 5k and l).

## Conclusions

In summary, a PEDOT-coated/embedded  $\text{Bi}_2\text{Te}_3$  is successfully fabricated through a hydrothermal method followed by the polymerization of EDOT. Various characterizations and DFT calculations demonstrate that the embedded PEDOT enlarges the interlayer spacing and reduces the interlamellar interaction, thus improving the reaction kinetics of  $\text{Bi}_2\text{Te}_3$ . Meanwhile, the coating of PEDOT enhances structural stability, suppresses side reactions with the aqueous solution, and increases electronic conductivity. *Ex situ* tests demonstrate the insertion-type mechanism of  $\text{Bi}_2\text{Te}_3$ @PEDOT in both ZIBs and AIBs. The  $\text{Bi}_2\text{Te}_3$ @PEDOT electrode exhibits high discharge capacities of 385 and  $235 \text{ mA h g}^{-1}$  at  $0.2 \text{ A g}^{-1}$  in ZIBs and AIBs, respectively. Even at a high mass loading of  $10 \text{ mg cm}^{-2}$ ,  $\text{Bi}_2\text{Te}_3$ @PEDOT shows satisfactory rate performances and cycling stability. Furthermore, “rocking-chair” ZIBs and AIBs with the  $\text{Bi}_2\text{Te}_3$ @PEDOT anode offer high reversible capacities of  $110 \text{ mA h g}^{-1}$  at  $1.0 \text{ A g}^{-1}$  (ZIBs) and  $110 \text{ mA h g}^{-1}$  at  $0.5 \text{ A g}^{-1}$  (AIBs), respectively. This work extends the utilizing scope of layered bismuth-based materials and serves as a reference for bifunctional energy storage electrodes.

## Data availability

The data supporting this article have been included in the main text and ESI.†

## Author contributions

X. L.: writing – original draft, data curation; F. L.: writing – original draft, data curation; H. Y.: data curation, investigation; Y. D.: formal analysis, resources, software; L. C.: investigation; T. S.: investigation; Y. P.: resources, software; X. W.: project administration, funding acquisition; B. L.: writing – review & editing, conceptualization, supervision; Y. X.: writing – review & editing, conceptualization, supervision; X. W.: writing – review & editing, project administration, funding acquisition. X. L. and F. L. contributed equally to this work.

## Conflicts of interest

There are no conflicts to declare.

## Acknowledgements

This work was supported by the Natural Science Foundation of China (52102312), Scientific Research Project of Education Department of Hunan Province (23C0047), and National Key R &





D Program of China (2021YFB2400400). The authors would like to thank Xiao Ming Li from SCI-GO (<http://www.sci-go.com>) for help with the XPS analysis.

## References

- M. Li, X. P. Wang, J. S. Meng, C. L. Zuo, B. K. Wu, C. Li, W. Sun and L. Q. Mai, *Adv. Mater.*, 2024, **36**, 2308628.
- Z. N. Ju, Q. Zhao, D. L. Chao, Y. Hou, H. G. Pan, W. P. Sun, Z. Y. Yuan, H. Li, T. Y. Ma, D. W. Su and B. H. Jia, *Adv. Energy Mater.*, 2022, **12**, 2201074.
- J. Liu, K. Wang, Y. Sun, H. Li, X. Han, X. Duan, Z. Huang and T. Ma, *Nano Energy*, 2025, **136**, 110764.
- C. Luo, H. Lei, Y. Xiao, X. Nie, Y. Li, Q. Wang, W. Cai, C. Dai, M. Yao, Y. Zhang and D. Yuan, *Energy Mater.*, 2024, **4**, 400036.
- X. Liu, B. Xu, S. Deng, J. Han, Y. An, J. Zhao, Q. Yang, Y. Xiao and C. Fang, *Carbon Energy*, 2024, **6**, e603.
- G. Zeng, Q. Sun, S. Horta, P. R. Martínez-Alanis, P. Wu, J. Li, S. Wang, M. Ibáñez, Y. Tian, L. Ci and A. Cabot, *Energy Environ. Sci.*, 2025, **18**, 1683–1695.
- W. Jiang, K. Zhu, W. Xie, Z. Wang, Z. Ou and W. Yang, *Chem. Sci.*, 2024, **15**, 2601–2611.
- Y. Zhang, Z. Huang, L. Lei, H. Fan, X. Han, H. Li and T. Ma, *Adv. Energy Mater.*, 2025, **15**, 2404732.
- F. Xiankai, X. Kaixiong, Z. Wei, D. Weina, Z. Hai, C. Liang and C. Han, *Carbon Energy*, 2024, **6**, e536.
- B.-H. Xiao, K. Xiao, J.-X. Li, C.-F. Xiao, S. Cao and Z.-Q. Liu, *Chem. Sci.*, 2024, **15**, 11229–11266.
- G. Zeng, Q. Sun, S. Horta, S. Wang, X. Lu, C. Y. Zhang, J. Li, J. Li, L. Ci, Y. Tian, M. Ibáñez and A. Cabot, *Adv. Mater.*, 2024, **36**, 2305128.
- B. Long, X. Ma, L. Chen, T. Song, Y. Pei, X. Wang and X. Wu, *Adv. Funct. Mater.*, 2024, **34**, 2411430.
- S. Gong, M. Zhu, Y. Zhou, R. Li, J. Zhang, X. Jia, D. Chao and C. Wang, *Chem. Sci.*, 2024, **15**, 19870–19885.
- J. Shi, Y. Hou, Z. Liu, Y. Zheng, L. Wen, J. Su, L. Li, N. Liu, Z. Zhang and Y. Gao, *Nano Energy*, 2022, **91**, 106651.
- H. Liu, K. Zhang, S. Wang and X. Cai, *Small*, 2023, **20**, 2310835.
- Q. Lei, J. Zhang, Z. Liang, Y. Yue, Z. Ren, Y. Sun, Z. Yao, J. Li, Y. Zhao, Y. Yin, P. Huai, Z. Lv, J. Li, Z. Jiang, W. Wen, X. Li, X. Zhou and D. Zhu, *Adv. Energy Mater.*, 2022, **12**, 2200547.
- D. Yu, Z. Wei, X. Zhang, Y. Zeng, C. Wang, G. Chen, Z. X. Shen and F. Du, *Adv. Funct. Mater.*, 2020, **31**, 2008743.
- S. Li, D. Yu, J. Liu, N. Chen, Z. Shen, G. Chen, S. Yao and F. Du, *Adv. Sci.*, 2023, **10**, 2206836.
- M. Han, Y. Qian, X. Li, N. Wang, T. Song, L. Liu, X. Wang, X. Wu, M.-K. Law and B. Long, *J. Colloid Interface Sci.*, 2023, **645**, 483–492.
- B. Long, Q. Zhang, T. Duan, T. Song, Y. Pei, X. Wang, C. Zhi, X. Wu, Q. Zhang and Y. Wu, *Adv. Sci.*, 2022, **9**, 2204087.
- D. Ling, Q. Wang, G. Tian, H. Yu, D. Zhang and Q. Wang, *ACS Nano*, 2023, **17**, 25222–25233.
- Q. Wang, M. Wang, L. Wen, W. Zeng, B. Ge, C. Zhang, Y. Yue and S. Wang, *Adv. Funct. Mater.*, 2023, **34**, 2214506.
- X. Wang, F. Zhou, Q. Liang, Q. Zhang, Y. Zhu, Z. Xiao and L. Wang, *Adv. Funct. Mater.*, 2024, **34**, 2408203.
- B. Long, X. Ma, L. Chen, T. Song, Y. Pei, X. Wang and X. Wu, *Adv. Funct. Mater.*, 2024, **34**, 2411430.
- S. Li, Y. Liu, X. Zhao, Q. Shen, W. Zhao, Q. Tan, N. Zhang, P. Li, L. Jiao and X. Qu, *Adv. Mater.*, 2021, **33**, e2007480.
- G. Zhang, T. Wu, H. Zhou, H. Jin, K. Liu, Y. Luo, H. Jiang, K. Huang, L. Huang and J. Zhou, *ACS Energy Lett.*, 2021, **6**, 2111–2120.
- W. Bi, G. Gao, G. Wu, M. Atif, M. S. AlSalhi and G. Cao, *Energy Storage Mater.*, 2021, **40**, 209–218.
- J. Feng, Z. Zhuang, Y. Zhou and C. Li, *Adv. Funct. Mater.*, 2024, **34**, 2315188.
- G. Wang, F. Meng, Y. Chen, A. Lotnyk and X. Shen, *Adv. Sci.*, 2024, **11**, e2308056.
- X. Liu, Y. Si, K. Li, Y. Xu, Z. Zhao, C. Li, Y. Fu and D. Li, *Energy Storage Mater.*, 2021, **41**, 255–263.
- C. Zheng, Z. Guo, B. Jian, Z. Chen, J. Zhong, N. Li and S. Huang, *Chem. Eng. J.*, 2023, **475**, 146408.
- S. Wang, Y. Qiao, X. Liu, S. Zhu, Y. Zheng, H. Jiang, Y. Zhang, J. Shen, Z. Li, Y. Liang, Z. Cui, P. K. Chu and S. Wu, *Adv. Funct. Mater.*, 2022, **33**, 2210098.
- X. B. Liao, C. L. Pan, H. X. Yan, Y. Zhu, Y. S. Pan and C. J. Yin, *Chem. Eng. J.*, 2022, **440**, 135930.
- K. Kim, M. Kim, H. Lee, D. W. Chung and J. Kim, *Small*, 2024, **20**, e2402341.
- S. Chong, L. Yuan, Q. Zhou, Y. Wang, S. Qiao, T. Li, M. Ma, B. Yuan and Z. Liu, *Small*, 2023, **19**, 2303985.
- Y. Wu, Q. Zong, Y. Zhuang, Q. Wang, C. Liu, Q. Zhang, D. Tao, J. Zhang, J. Wang and G. Cao, *Chem. Eng. J.*, 2024, **491**, 152064.
- D. Bin, W. Huo, Y. Yuan, J. Huang, Y. Liu, Y. Zhang, F. Dong, Y. Wang and Y. Xia, *Chem*, 2020, **6**, 968–984.
- X. Tan, F. Zhang, D. Chen, P. Wang, Y. Liu, C. Meng and Y. Zhang, *Chem. Eng. J.*, 2024, **489**, 151119.
- X. Tan, F. Zhang, D. Chen, J. n. Gong, J. Sun, C. Meng and Y. Zhang, *J. Colloid Interface Sci.*, 2024, **669**, 2–13.
- K. Zhu, W. Jiang, Z. Wang, W. Li, W. Xie, H. Yang and W. Yang, *Angew Chem. Int. Ed. Engl.*, 2023, **62**, e202213368.
- H. Geng, M. Cheng, B. Wang, Y. Yang, Y. Zhang and C. C. Li, *Adv. Funct. Mater.*, 2019, **30**, 1907684.
- L. Chen, H. Nie, S. Zhou, G. Cao and A. Pan, *Sci. China Mater.*, 2023, **66**, 3453–3460.
- Y. Hou, P. Ma, F. Long, M. Liu, Y. Zheng, L. Sun, J. Shi, K. Niu, J. Su, Y. Ma and Y. Gao, *ACS Nano*, 2024, **18**, 27358–27371.
- S. Hu, X. Huang, L. Zhang, G. Li, S. Chen, J. Zhang and X. Liu, *Adv. Funct. Mater.*, 2023, **33**, 2214161.
- Y. Song, Q. Pan, H. Lv, D. Yang, Z. Qin, M. Y. Zhang, X. Sun and X. X. Liu, *Angew. Chem., Int. Ed.*, 2021, **60**, 5718–5722.
- X. Mu, Y. Song, Z. Qin, J. Meng, Z. Wang and X.-X. Liu, *Chem. Eng. J.*, 2023, **453**, 139575.

